Physics of the Earth and Planetary Interiors 229 (2014) 40–54

Contents lists available at ScienceDirect

Physics of the Earth and Planetary Interiors

journal homepage: www.elsevier.com/locate/pepi

Stagnant lid convection in 3D-Cartesian geometry: Scaling laws and applications to icy moons and dwarf planets

Frédéric Deschamps [a,*], Ja-Ren Lin [b]

[a] Institute of Earth Sciences, Academia Sinica, 128 Academia Road Sec. 2, Nangang, Taipei 11529, Taiwan
[b] Jin-Hua Junior High-School, 32 Xinsheng South Road Sec. 2, Da'an, Taipei 106, Taiwan

ARTICLE INFO

Article history:
Received 27 February 2013
Received in revised form 20 December 2013
Accepted 7 January 2014
Available online 17 January 2014
Edited by M. Jellinek

Keywords:
Thermal convection
Stagnant lid
Icy moons
Pluto

ABSTRACT

We conducted numerical experiments of stagnant lid thermal convection in 3D-Cartesian geometry, and use these experiments to derive parameterizations for the average internal temperature, heat flux, and stagnant lid thickness. Our experiments suggest that the non-dimensional temperature jump across the bottom thermal boundary layer (TBL) is well described by $(1-\theta_m)=1.23(\Delta T_v/\Delta T)$, where θ_m is the non-dimensional average temperature of the convective sublayer, and $\Delta T_v/\Delta T$ a viscous temperature scale defined as the inverse of the logarithmic temperature derivative of viscosity. Due to the presence of the stagnant lid at the top of the fluid, the frequency of the time-variations of the surface heat flux is much lower than those of the bottom heat flux. The Nusselt number, measuring the heat transfer, is well explain by $Nu=1.46Ra_m^{0.270}(\Delta T_v/\Delta T)^{1.21}$, where Ra_m is the effective Rayleigh number. This result indicates that the heat flux through the outer ice shells of large icy moons and dwarf planets is larger than that predicted by scalings in 2D-Cartesian geometry by 20–40%. We then apply our parameterizations to the dynamics of the outer ice I shells of icy moons and dwarf planets. As pointed out in previous studies, our calculations indicate that the presence of volatile in the primordial ocean of these bodies strongly reduces the vigor of convection within their outer ice I shell, the heat transfer through these shells, and the tectonic activity at their surface. Furthermore, thicker ice I layers may be achieved in bodies having low (0.7 m/s^2) gravity acceleration (*e.g.*, Pluto), than in bodies having larger (1.3 m/s^2 and more) gravity acceleration (*e.g.*, Europa, Ganymede, and Titan). Decrease in the surface temperature increases the thickness of the stagnant lid, which may result in a stronger lithosphere, and thus in fewer tectonic activity. Our parameterizations may also be used as boundary conditions at zero curvature to build parameterizations in spherical geometry.

1. Introduction

In fluids with large thermal viscosity contrast (typically, 10^4 and more), thermal convection operates in the stagnant lid regime (*e.g.*, Davaille and Jaupart, 1993; Solomatov, 1995; Moresi and Solomatov, 1995; Deschamps and Sotin, 2000). In this mode of convection, a rigid lid is generated at the top of the fluid, and convection is confined below this lid. Due to the temperature drop in the top part of the fluid, the viscosity strongly increases and both the horizontal and vertical components of the velocity go to zero. The dominant mode of heat transfer in the lid switches to conduction, and compared to isoviscous convection, the heat transfer throughout the whole fluid layer is severely reduced. For a volumetrically heated fluid, Davaille and Jaupart (1993) have shown that most of the viscosity contrast is accommodated by the conductive lid, and that the temperature jump across the thermal boundary layer (TBL) located at the top of the convecting sublayer is proportional to a viscous temperature scale, a result confirmed by numerical experiments (Grasset and Parmentier, 1998). This suggests that the convective sublayer behaves nearly as an isoviscous fluid. For a fluid heated from below, numerical experiments indicate that the convective sublayer also behaves as an isoviscous fluid with a good approximation (Moresi and Solomatov, 1995).

Stagnant lid convection may play a significant role in the cooling of large icy moons and dwarf planets of the outer solar system. The radial structures of these bodies may include a thin (100–250 km) outer ice I layer. If it is thick enough, this layer may become unstable and convect. Because the viscosity of ice is strongly temperature-dependent (*e.g.*, Goodman et al., 1981; Weertman, 1983), stagnant lid convection is likely to occur in the outer ice I layer, thus limiting the heat flux that can be extracted from the silicate core (or mantle). Together with the presence of volatiles, which reduces the liquidus of water, this may strongly influences the crystallization of the primordial ocean, leading to the presence of a sub-surface ocean beneath the ice I layer (*e.g.*, Grasset et al.,

* Corresponding author. Tel.: +886 227839910.
E-mail address: frederic@earth.sinica.edu.tw (F. Deschamps).

0031-9201/$ - see front matter © 2014 Elsevier B.V. All rights reserved.
http://dx.doi.org/10.1016/j.pepi.2014.01.002

2000; Deschamps and Sotin, 2001; Spohn and Schubert, 2003; McKinnon, 2006; Mitri and Showman, 2008). Sub-surface oceans may be a common feature of large differentiated icy bodies (Hussmann et al., 2006), including Ceres (McCord and Sotin, 2005). The observation that the convective sublayer behaves nearly as an isoviscous fluid was used to approximate icy shells with isoviscous layers overlain by thick rigid lids, allowing the use of heat flux parameterizations built for isoviscous fluid to model the thermal histories of icy moons and dwarf planets with a reasonable accuracy. A more detailed description of these evolutions however requires parameterizations directly built from stagnant lid convection experiments.

Here, we perform series of numerical experiments of stagnant lid convection in 3D-Cartesian geometry, from which we infer parameterizations for heat flux and temperature. Parameterizations built from experiments in 3D-Cartesian geometry have two main interests. First, they may be directly applied to outer ice layers of icy moons and dwarf planet, since these layers have small curvatures. Second, they can be used as a boundary condition (with zero curvature) for calculations in spherical geometry.

2. Physical model

We performed series of numerical experiments of thermal convection, in which we solved the conservation equations of mass, momentum, and energy for an incompressible, infinite Prandtl number fluid in 3D-Cartesian geometry using StagYY (Tackley, 2008). At each time step, the conservation equations are solved using a Jacobi relaxation method. Convergence of the momentum and pressure equation is speeded up using a multigrid method (*e.g.*, Wesseling, 1992). Time-stepping in the conservation of energy is achieved by an explicit MPDATA (Smolarkiewicz, 1984) algorithm for advective terms, and a second-order finite difference scheme for diffusive terms.

The viscosity η strongly varies with the temperature T following an exponential law,

$$\eta(x,y,z) = \eta_0 \exp\left[-\gamma \frac{(T(x,y,z) - T_0)}{\Delta T}\right], \quad (1)$$

where η_0 and T_0 are the reference (*e.g.*, the surface values of) viscosity and temperature, ΔT is the super-adiabatic temperature difference between the bottom and the top of the fluid, and γ a parameter that controls the amplitude of the viscosity variations. Following Eq. (1), the top to bottom viscosity ratio is $\Delta\eta = \exp(\gamma)$. Thanks to a new pressure interpolation scheme in the prolongation operator of the multigrid cycle, StagYY can handle very high viscosity ratios, up to 10^{19} (Tackley, 2008). This scheme is somewhat equivalent to a matrix-dependent prolongation operator (Wesseling, 1992), which is well adapted to problems where scalar parameters of the equations (*e.g.*, the viscosity) strongly vary throughout the domain.

The vigor of convection is controlled by the Rayleigh number,

$$Ra = \frac{\alpha \rho g \Delta T D^3}{\eta K}, \quad (2)$$

where α, ρ, and κ are the fluid thermal expansion, density, and thermal diffusivity, g is the acceleration of gravity, and D the thickness of the domain. Note that ΔT and D are used as temperature and length scale, respectively. Because viscosity varies with temperature throughout the system, the definition of the Rayleigh number is non-unique. It is convenient to define a reference Rayleigh number calculated at a reference temperature common to all calculations, *e.g.*, the surface temperature, which is always equal to T_0 in our experiments. Another frequently used reference Rayleigh number is the median Rayleigh number $Ra_{1/2}$, calculated at the median temperature $T_{1/2} = T_0 + \Delta T/2$. Beneath the stagnant lid, the fluid is significantly hotter and less viscous than in the lid, and it is useful to define a Rayleigh number of the well-mixed interior (hereafter referred to as effective Rayleigh number), Ra_m, calculated with the average temperature T_m of the well-mixed convective interior. The effective Rayleigh number thus implicitly takes into account the effects of viscosity variations. In all our experiments, we prescribe the surface Rayleigh number Ra_0, and calculate Ra_m *a posteriori* with

$$Ra_m = Ra_0 \exp(\gamma \theta_m), \quad (3)$$

where $\theta_m = (T_m - T_0)/\Delta T$ is the non-dimensional temperature of the well-mixed interior. This temperature is an output observable that we measure from the adiabatic part of the horizontally averaged profile of temperature. Another important observable is the Nusselt number Nu, measuring the efficiency of the convective heat transfer relatively to the conductive heat transfer, and which is given by the ratio between the observed heat flux and the global conductive heat flux $\Phi_{cond} = k\Delta T/D$.

Calculations are performed in 3D-Cartesian boxes with horizontal to vertical aspect ratio equal to 4. Scalar quantities (temperature, pressure, viscosity) are calculated at the middle of each cell, whereas vectorial quantities (in our case, velocity) are calculated on the side of each cell. The top and bottom boundaries are free slip and isothermal, and we impose reflective boundary conditions on the sidewalls. To test the influence of the aspect ratio, we conducted a series of experiments with aspect ratio between 1 and 8 for two cases (Table 1). These experiments indicate that for aspect ratio larger than 2, the average properties of the fluid (average temperature, Nusselt number, and root mean square of velocity) are nearly independent of the aspect ratio. We used different grid resolution, $npx \times npy \times npz$, depending on the expected value of the effective Rayleigh number. For effective Rayleigh number smaller than 10^7 we fixed the grid resolution to $128 \times 128 \times 64$ points. For larger Rayleigh numbers, we increased the resolution to $256 \times 256 \times 128$ or $384 \times 384 \times 192$ points, depending on the case (Table 2). Note that to better describe the thermal boundary layers, the grid is vertically refined at the top and at the bottom of the domain. The initial condition for the temperature consists of 3D-random perturbations, and the calculations are carried on until a quasi-stationary state is reached. In some cases, the temperature condition is given by the temperature distribution from a previous experiment having converged with lower Rayleigh number. In the ranges of Rayleigh number and viscosity contrast we explored, the flow is time-dependent, reaching a quasi-stationary state after a period of time. During this phase, the average temperature and the Nusselt number oscillate around values that are constant in time. For each case, we determine these values by averaging the temperature and the Nusselt number over several oscillations.

Table 1
Influence of aspect ratio.

$\Delta\eta$	Ra_0	r_a	Resolution	θ_m	Nu	RMS(V)
10^5	31.62	1	$64 \times 64 \times 64$	0.88824	3.197	146.34
–	–	2	$128 \times 128 \times 64$	0.89166	3.033	145.38
–	–	4	$128 \times 128 \times 64$	0.89427	3.078	146.16
–	–	8	$256 \times 256 \times 64$	0.89376	3.104	144.96
10^6	10.00	1	$64 \times 64 \times 64$	0.91087	3.541	253.33
–	–	2	$128 \times 128 \times 64$	0.91303	3.410	255.19
–	–	4	$128 \times 128 \times 64$	0.91163	3.452	248.92
–	–	8	$256 \times 256 \times 64$	0.91068	3.449	249.97

Input parameters are the top to bottom thermal viscosity ratio, $\Delta\eta$, the surface Rayleigh number, Ra_0, and the aspect ratio r_a. Output observables are the non-dimensional temperature of the well-mixed interior, θ_m, the Nusselt number, Nu, and the root mean square of the velocity, RMS(V).

Table 2
Stagnant lid convection experiments in 3D-Cartesian geometry.

$\Delta\eta$	Ra_0	Resolution	θ_m	Nu	δ_{lid}	Ra_m
3.2×10^4	89.47	$128 \times 128 \times 64$	0.87894	3.469	0.224	8.15×10^5
–	178.89	$128 \times 128 \times 64$	0.88175	4.177	0.188	1.68×10^6
–	313.05	$128 \times 128 \times 64$	0.88123	4.843	0.162	2.92×10^6
–	894.65	$256 \times 256 \times 128$	0.88370	6.373	0.129	8.56×10^6
5.6×10^4	67.61	$128 \times 128 \times 64$	0.88871	3.485	0.226	1.12×10^6
–	135.22	$128 \times 128 \times 64$	0.88997	4.248	0.186	2.27×10^6
10^5	31.62	$128 \times 128 \times 64$	0.89427	3.078	0.257	9.36×10^5
–	50.60	$128 \times 128 \times 64$	0.89523	3.563	0.224	1.51×10^6
–	79.06	$128 \times 128 \times 64$	0.89323	4.074	0.196	2.31×10^6
–	126.49	$128 \times 128 \times 64$	0.89238	4.538	0.176	3.66×10^6
–	199.22	$256 \times 256 \times 128$	0.89248	5.192	0.158	5.78×10^6
–	316.23	$256 \times 256 \times 128$	0.89359	5.618	0.142	9.29×10^6
–	1011.89	$256 \times 256 \times 128$	0.89337	7.829	0.108	2.96×10^7
1.8×10^5	37.71	$128 \times 128 \times 64$	0.89985	3.642	0.221	2.02×10^6
–	169.68	$256 \times 256 \times 128$	0.89773	5.476	0.152	8.86×10^6
3.2×10^5	17.68	$128 \times 128 \times 64$	0.90203	3.290	0.246	1.63×10^6
–	56.57	$128 \times 128 \times 64$	0.90183	4.423	0.183	5.22×10^6
–	176.78	$256 \times 256 \times 128$	0.90243	6.071	0.139	1.64×10^7
5.6×10^5	13.36	$128 \times 128 \times 64$	0.90896	3.361	0.243	2.24×10^6
–	42.76	$128 \times 128 \times 64$	0.90603	4.556	0.180	6.90×10^6
10^6	4.50	$128 \times 128 \times 64$	0.91020	2.733	0.299	1.30×10^6
–	10.00	$128 \times 128 \times 64$	0.91163	3.452	0.238	2.95×10^6
–	16.00	$128 \times 128 \times 64$	0.91171	3.912	0.211	4.72×10^6
–	25.00	$128 \times 128 \times 64$	0.90968	4.416	0.186	7.18×10^6
–	40.00	$256 \times 256 \times 128$	0.91108	5.013	0.169	1.17×10^7
–	63.00	$256 \times 256 \times 128$	0.91172	5.814	0.150	1.86×10^7
–	100.00	$256 \times 256 \times 128$	0.91048	6.216	0.136	2.90×10^7
3.2×10^6	17.89	$256 \times 256 \times 128$	0.91678	4.973	0.172	1.65×10^7
–	41.93	$256 \times 256 \times 128$	0.91805	6.164	0.140	3.93×10^7
10^7	0.34	$128 \times 128 \times 64$	0.92208	2.162	0.386	1.08×10^6
–	0.63	$128 \times 128 \times 64$	0.92203	2.528	0.331	1.80×10^6
–	3.16	$256 \times 256 \times 128$	0.92328	3.887	0.219	9.18×10^6
–	10.12	$256 \times 256 \times 128$	0.92332	5.275	0.164	2.94×10^7
–	31.62	$256 \times 256 \times 128$	0.92348	7.011	0.124	9.21×10^7
3.2×10^7	7.07	$256 \times 256 \times 128$	0.92902	5.950	0.148	6.64×10^7
–	17.68	$384 \times 384 \times 192$	0.92597	7.527	0.114	1.57×10^8
10^8	0.06	$128 \times 128 \times 64$	0.93018	2.094	0.405	1.66×10^6
–	0.10	$128 \times 128 \times 64$	0.93244	2.429	0.352	2.88×10^6
–	1.00	$256 \times 256 \times 128$	0.93301	4.445	0.196	2.91×10^7
–	1.60	$256 \times 256 \times 128$	0.93299	5.021	0.175	4.66×10^7
–	3.20	$256 \times 256 \times 128$	0.93282	5.993	0.148	9.28×10^7
10^9	0.04	$256 \times 256 \times 128$	0.94076	3.143	0.279	1.30×10^7
–	1.00	$384 \times 384 \times 192$	0.93662	7.145	0.122	2.72×10^8
10^{10}	0.008	$256 \times 256 \times 128$	0.94653	3.225	0.276	2.34×10^7
–	0.08	$384 \times 384 \times 192$	0.94485	5.828	0.153	2.25×10^8

Input parameters are the top to bottom thermal viscosity ratio, $\Delta\eta$, and the surface Rayleigh number, Ra_0. Output observables are the non-dimensional temperature of the well-mixed interior, θ_m, the Nusselt number, Nu, and the thickness of the stagnant lid, δ_{lid}, measured from the tangent at the point of inflexion of the horizontally averaged vertically advected heat flux ($u_z T$). Output observable are averaged out in time over a few oscillations after quasi-stationary state is reached. For convenience, we also list the effective Rayleigh number Ra_m (Eq. (3)).

3. Results from numerical experiments

We performed 45 experiments using the setup described in Section 2 and varying the bottom to top thermal viscosity contrast $\Delta\eta$ between 3.2×10^4 and 10^{10} (Table 2). All 45 experiments are in the stagnant lid regime. A consequence of the stagnant lid is that the vertically advected heat cancels out at the top of the system. This property may be used to infer the thickness of the stagnant lid (see below). Another consequence of the stagnant lid is that the top part of the temperature profile is purely conductive. This results in a non-dimensional temperature of the well-mixed interior θ_m much larger than 0.5 (in all our experiments θ_m is larger than 0.85), and in a reduced temperature jump across the bottom thermal boundary layer. A close examination at Table 2 indicates that the temperature of the well-mixed interior is independent of the Rayleigh number. The Nusselt number, on the contrary, increases with increasing effective Rayleigh number.

3.1. Flow pattern

Fig. 1 plots temperature isosurfaces for selected cases with different effective Rayleigh number. The flow is restricted to a layer located beneath the stagnant lid. In the stagnant lid, thermals consist of horizontal surfaces slightly deflected upwards or downwards in regions where hot plumes or cold downwellings are present in the underlying flow. For the aspect ratio we used and in the range of viscosity contrast and surface Rayleigh number we prescribed (corresponding to effective Rayleigh number Ra_m between 10^6 and 10^8), the convective pattern that develops beneath the conductive lid forms an asymmetric network of cells with irregular shapes (often referred to as spokes pattern), as observed in analogical (White, 1988) and numerical (Ogawa et al., 1991) experiments. Each cell consists in a central hot plume surrounded by interconnected downwelling sheets bounding adjacent cells. The hot plumes of adjacent cells are interconnected by hot

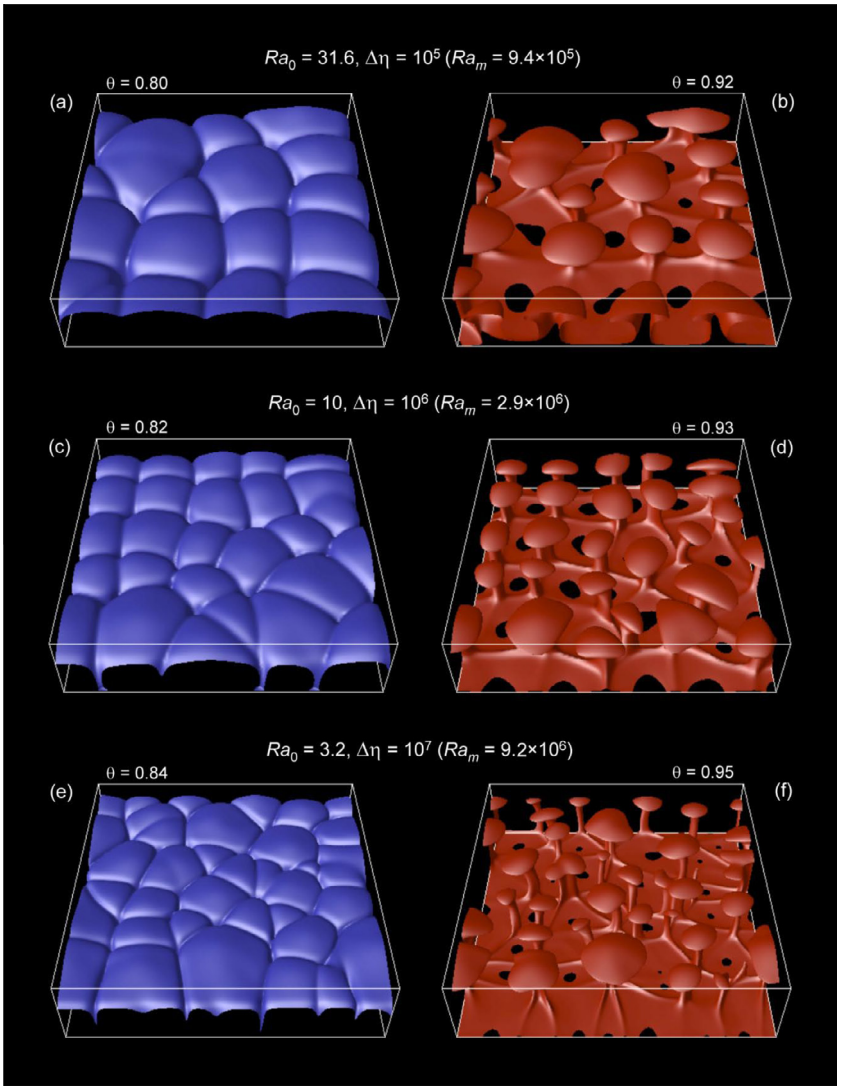

Fig. 1. Snapshots of three selected cases. For each case, a cold (left column) and a hot (right column) isosurface are shown. Snapshots are taken after the quasi-stationary state has been reached. Cases are, from top to bottom, $Ra_0 = 31.6$ and $\Delta\eta = 10^5$ ($Ra_m = 9.4 \times 10^5$), $Ra_0 = 10$ and $\Delta\eta = 10^6$ ($Ra_m = 2.9 \times 10^6$), and $Ra_0 = 3.2$ and $\Delta\eta = 10^7$ ($Ra_m = 9.2 \times 10^6$).

ridges. Cells with more regular shapes (hexagons or squares) may be obtained for boxes with smaller (<3) aspect ratio and at lower values of $\Delta\eta$ and $Ra_{1/2}$ (White, 1988; Christensen and Harder, 1990; Ogawa et al., 1991), but for such setups the stagnant lid regime may not be fully developed. In the range of Rayleigh number we explored, the flow is time-dependent. The size and shape of the cells vary in time, but the time-averaged number and size of these cells remain constant, as shown in Fig. 2 for the case $Ra_0 = 3.2$ and $\Delta\eta = 10^7$ (corresponding to $Ra_m = 9.2 \times 10^6$).

3.2. Time-variation of the average heat-flux

Small time variations in the flow pattern are associated with oscillations of the horizontally-averaged heat flux around constant values. Fig. 3, which plots variations of the heat flux at the top and at the bottom of the box for selected cases, indicates that the frequency of the heat flux oscillations increase with increasing effective Rayleigh number. Furthermore, for a given effective Rayleigh number, this frequency increases with decreasing thermal viscosity contrast (Fig. 3b and c). In all cases, however, the time averaged surface and basal heat flux are equal to one another, as required by conservation of energy. By contrast, the details of the heat flux oscillations at the top and at the bottom of the fluid differ significantly. The amplitude of oscillations at the top of the fluid are slightly smaller than (but still comparable to) those at the bottom of the fluid. At the bottom, the peak-to-peak amplitude relative to the time-averaged value varies between 1% and 7%, depending on the case, and is 3% on average. At the top, the relative peak-to-peak amplitude varies between 1% and 4%, and is 2% on average. More importantly, the frequency of the heat flux oscillations is much larger at the bottom of the fluid than below its surface. The stagnant lid therefore acts as a low-frequency pass filter for the variations in the heat flux, *i.e.*, the high-frequency oscillations of the heat flux generated at the bottom of the fluid are filtered out by the lid.

The dependence of the frequency of heat flux oscillations on the Rayleigh number and on the viscosity contrast, and their variations from top to bottom, may be explained by differences in the time needed for the growth of instabilities in the top and bottom TBL. When quasi-equilibrium is reached, the time-averaged conductive heat flux should be equal to the half-space cooling solution,

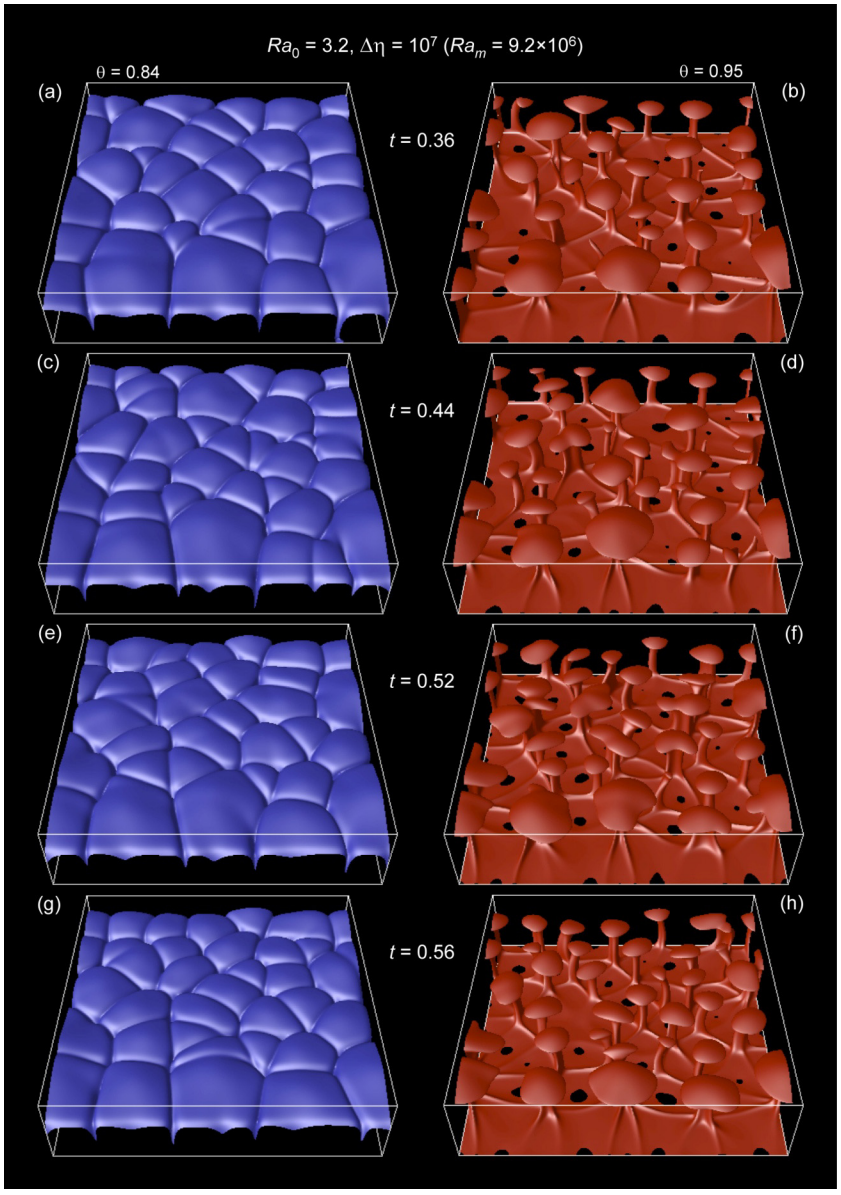

Fig. 2. Snapshots of the case $Ra_0 = 3.2$ and $\Delta\eta = 10^7$ ($Ra_m = 9.2 \times 10^6$) at four different times.

$$\bar{\Phi} = \frac{2k\Delta T_c}{\sqrt{\pi\kappa t_c}}, \tag{4}$$

where ΔT_c is the temperature jump across the conductive domain (in our case, either the bottom TBL, or the sum of the stagnant lid and the top TBL, hereafter referred to as top conductive layer), κ the thermal diffusivity, and t_c the time for the growth of instabilities. Solving for Eq. (4), and using the total thickness of the box D, the diffusion time D^2/κ, and the super-adiabatic temperature jump ΔT as characteristic length, time, and temperature, the non-dimensional time for the growth of instabilities in the bottom TBL and top conductive layers are

$$t^*_{bot} = \frac{4}{\pi}\left(\frac{\delta T_{bot}}{Nu}\right)^2, \tag{5a}$$

and

$$t^*_{top} = \frac{4}{\pi}\left(\frac{\delta T_{top}}{Nu}\right)^2, \tag{5b}$$

respectively, where Nu is the time-averaged Nusselt number (Table 2), δTbot the non-dimensional temperature jump across the bottom TBL, and δTtop the non-dimensional temperature jump across the top conductive layer (stagnant lid + top TBL). Note that Eq. (5b) implicitly assumes that the stagnant lid is an upward extension of the top TBL. With a good approximation, $\delta T_{bot} = (1 - \theta_m)$ and $\delta T_{top} = \theta_m$, where θm is the average temperature in the well mixed interior (Table 2). The ratios $\delta T_{bot}/Nu$ and $\delta T_{top}/Nu$ are also good approximations for the thickness of the bottom TBL, δbot, and for the cumulated thickness of the top TBL and of the stagnant lid, δtop, respectively. A careful examination at Table 2 shows that Nu increases with the effective Rayleigh number Ram and, for a given value of Ram, decreases with the thermal viscosity contrast, whereas θm increases with the thermal viscosity contrast but does not depend on Ram (these trends are further quantified in Section 4). On the whole, both $\delta T_{bot}/Nu$ and $\delta T_{top}/Nu$, and therefore t^*_{bot} and t^*_{top}, decrease with increasing Ram and decreasing thermal viscosity contrast. Furthermore, δTbot is smaller than δTtop by about an order of magnitude or more (in our experiments,

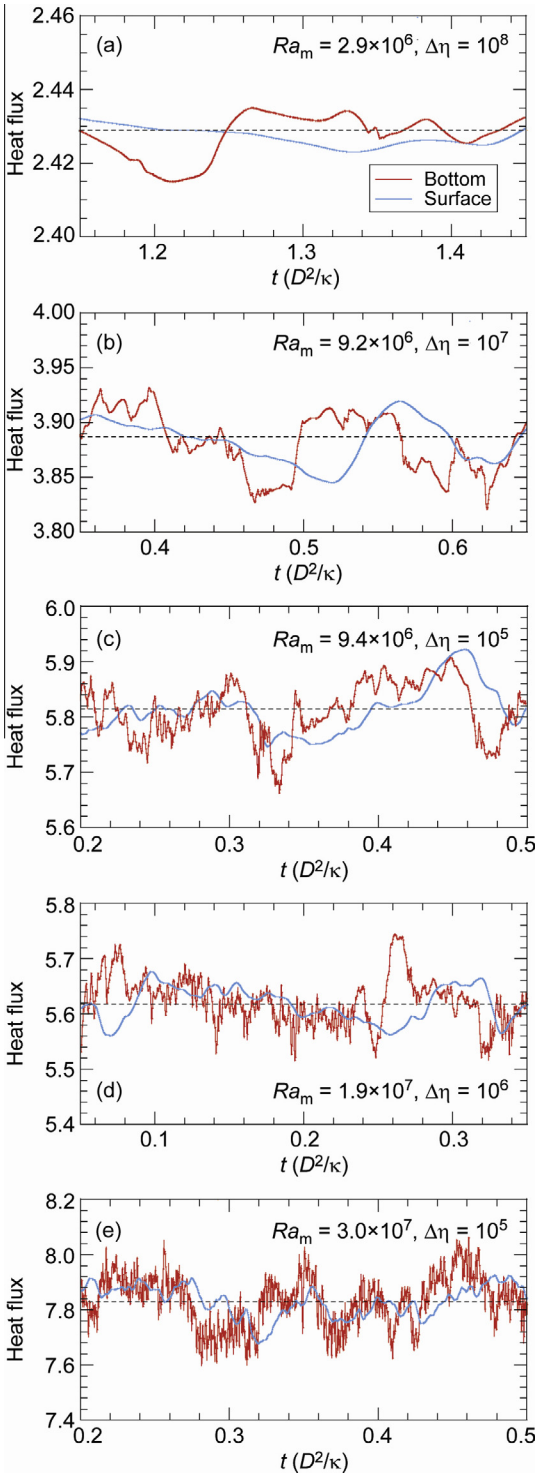

Fig. 3. Time evolution of the non-dimensional surface and basal heat flux for 5 cases (the effective Rayleigh number increases from top to bottom panels). (a) $Ra_m = 2.9 \times 10^6$ and $\Delta\eta = 10^8$. (b) $Ra_m = 9.2 \times 10^6$ and $\Delta\eta = 10^7$. (c) $Ra_m = 9.4 - \times 10^6$ and $\Delta\eta = 10^5$. (d) $Ra_m = 1.9 \times 10^7$ and $\Delta\eta = 10^6$. (e) $Ra_m = 3.0 \times 10^7$ and $\Delta\eta = 10^5$.

$\delta T_{top}/\delta T_{bot}$ varies between about 7 for $\Delta\eta = 3.2 \times 104$, and 18 for $\Delta\eta = 1010$), which implies that t^*_{bot} is smaller than t^*_{top} by about two orders of magnitude and more. In other words, instabilities grow faster with increasing Ram and decreasing viscosity contrast, and they grow faster in the bottom TBL than in the top conductive layer.

Eqs. (5a) and (5b) qualitatively explains the differences observed in the frequencies of the heat flux oscillations, depending on the location, the Rayleigh number and the viscosity contrast. Practically, however, the shortest oscillations we observed in our experiments are larger than the values predicted by Eqs. (5a) and (5b) by about 30–50%. This discrepancy may be related to the fact that both existing plumes and new instabilities participate to the heat transfer, as pointed out for internally heated isoviscous fluids (Parmentier and Sotin, 2000; Deschamps et al., 2012). Alternatively, interactions between cold downwellings or hot plumes and the opposite TBL may influence the growth of instabilities in TBLs.

4. Scaling laws for stagnant lid regime

4.1. Temperature jump across and thickness of the bottom TBL

Analytical (Morris and Canright, 1984; Fowler, 1985), experimental (Davaille and Jaupart, 1993), and numerical (Solomatov, 1995; Moresi and Solomatov, 1995; Deschamps and Sotin, 2000) studies indicate that the temperature jump across the top thermal boundary layer is controlled by the thermal viscosity contrast through an appropriate viscous temperature scale,

$$\Delta T_v = \frac{\eta(T_m)}{\frac{d\eta}{dT}|_{T=T_m}}, \tag{6}$$

where T_m is the temperature of the well-mixed interior. Following Eq. (1), the viscous temperature scale in our experiment is related to the logarithmic thermal viscosity contrast through $\Delta T_v = \Delta T/\gamma$. For a bottom heated fluid, numerical experiments indicate that the temperature jump in the bottom TBL is also proportional to the viscous temperature scale (Deschamps and Sotin, 2000). The measure of the temperature jump across the bottom TBL is more direct and more accurate than that in the top TBL, which requires an accurate determination of the boundary between the lid and the top TBL. Our numerical experiments can be used to determine scaling laws for the temperature, and thus for the temperature jump in the bottom TBL. These experiments indicate that θ_m varies with the thermal viscosity contrast $\Delta\eta$ (and thus with γ), but is independent of the Rayleigh number. The non-dimensional temperature difference across the bottom TBL is well explained by (Fig. 4a)

$$(1 - \theta_m) = a_T\left(\frac{\Delta T_v}{\Delta T}\right), \tag{7}$$

where $a_T = 1.23 \pm 0.05$. The value of a_T was determined by a least-square fit of the data listed in Table 2, and its uncertainty was obtained assuming a relative uncertainty in the average temperature of 0.3%, corresponding to the average amplitude of the oscillations of the average temperature during the quasi-stationary phase. An interesting consequence of Eq. (7) is that the viscosity jump across the bottom TBL is independent of both the Rayleigh number and the thermal viscosity contrast, and is equal to $e^{1.23} = 3.4$.

The analytical study of Morris and Canright (1984) further indicates that the thickness of the top TBL below the stagnant lid also scales as the viscous temperature scale ΔT_v. A similar relationship may hold for the thickness of the bottom TBL, δ_{bot}, which may then be deduced from the cumulated thickness of the stagnant lid and top TBL, δ_{top}, following

$$\delta_{bot} = a_d\delta_{top}\left(\frac{\Delta T_v}{\Delta T}\right). \tag{8}$$

Assuming that $\delta_{top} = \theta_m/Nu$ and $\delta_{bot} = (1 - \theta_m)/Nu$, we calculated δ_{top} and δ_{bot} using the values of Nu and θ_m in Table 2, and found that δ_{top} and δ_{bot} fit Eq. (8) with $a_d = 1.36 \pm 0.1$ very well (Fig. 4b).

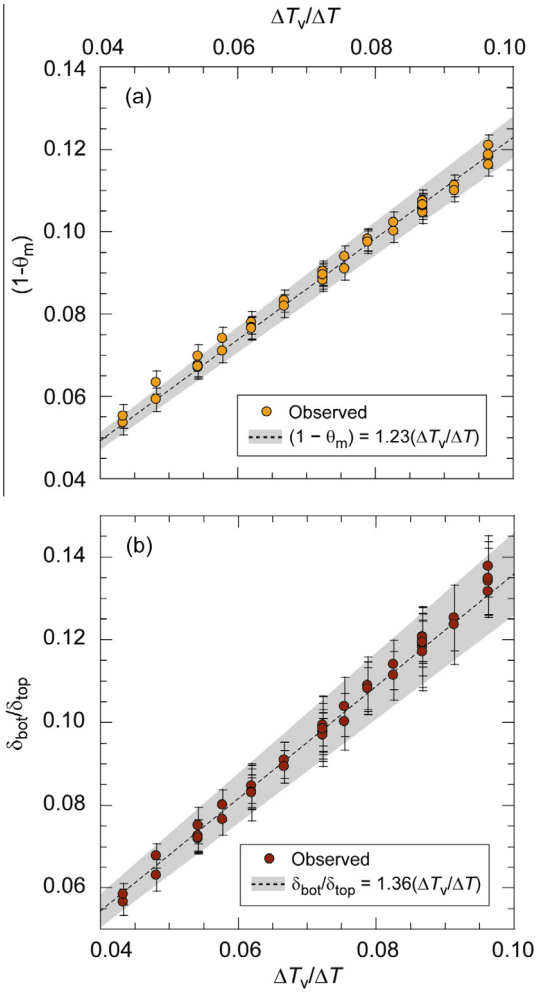

Fig. 4. (a) Average temperature in the well-mixed interior (Eq. (7)) as a function of the viscous temperature scale (Eq. (6)). The best fit model to Eq. (7) is indicated by the dashed line, and the shaded band covers one error bar around this best fit model. (b) Thickness of the bottom thermal boundary layer δ_{bot} (Eq. (8)) as a function of the viscous temperature scale. Plotted values are relative to the thickness of the top conductive layer (formed by the sum of the stagnant lid and the top thermal boundary layer), δ_{top}. The best fit model to Eq. (8) is indicated by the dashed line, and the shaded band covers one error bar around this best fit model.

It should be noted that Eqs. (7) and (8) and the parameter values we inverted for are not valid for small values of the viscous temperature scale, typically $\Delta T_v/\Delta T$ around 0.1 and larger. The reason is that for such values of the thermal viscosity contrast is too small (10^4 and less), and therefore convection is not in the stagnant lid regime.

4.2. Nusselt number

Large thermal viscosity contrasts have two opposite effects on the Nusselt number. The Nusselt number increases with the effective Rayleigh number, and thus implicitly with the thermal viscosity contrast. However, the presence of the stagnant conductive lid at the top of the system acts as an insulator, thus limiting the heat transfer towards the surface. This later effect dominates, and overall the Nusselt number strongly decreases with increasing thermal viscosity contrast, as noted in 2D-Cartesian numerical experiments (Christensen, 1984; Moresi and Solomatov, 1995; Deschamps and Sotin, 2000). For an isoviscous fluid, a TBL analysis indicates that the non-dimensional heat flux across a TBL scales as (Moore and Weiss, 1973)

$$Q_{adim} = aRa^b \delta T_{TBL}^c, \tag{9}$$

where δT_{TBL} is the temperature jump across the TBL. For stagnant lid convection, the temperature jump in the bottom TBL is well explained by Eq. (7). Furthermore, in Cartesian geometry, the energy conservation implies that the top and bottom horizontally averaged heat flux are equal. Replacing Ra by the effective Rayleigh number Ra_m, and δT_{TBL} by Eq. (7), one obtains an expression for the observed Nusselt number, *i.e.*,

$$Nu = aRa_m^b \left(\frac{\Delta T_v}{\Delta T}\right)^c. \tag{10}$$

To determine the values of a, b, and c, we inverted the values of Nu in Table 2 following Eq. (10) and using the generalized non-linear inversion method of Tarantola and Valette (1982). This method gives *a posteriori* uncertainties, provided that uncertainties in the data are prescribed. Here, we assumed a relative uncertainty in the Nusselt number of 2.0%, which again corresponds to the average amplitude of the oscillations of the Nusselt number during the quasi-stationary phase. We found $a = 1.46 \pm 0.06$, $b = 0.270 \pm 0.004$, and $c = 1.21 \pm 0.03$. Fig. 5 plots the reduced Nusselt number, defined as $Nu/(\Delta T_v/\Delta T)^{1.21}$, and shows that Eq. (10) with these parameter values explain very well the Nusselt number observed in our numerical experiments.

4.3. Thickness of the stagnant lid

A good estimate of the stagnant lid thickness, δ_{lid}, is given by the intersection between the tangent at the point of inflexion of the horizontally averaged profile of the vertically advected heat u_zT (where u_z is the vertical component of the velocity and T the temperature), and the origin axis $u_zT = 0$ (Davaille and Jaupart, 1993). We applied this method to our experiments (Table 2). Like the average temperature and the Nusselt number, the thickness of the stagnant lid oscillates around a constant value once a quasi-equilibrium is reached. The values of δ_{lid} listed in Table 2 are time-averaged over a few oscillations. The variance related to the oscillations is different for each case, and is on average equal to 2% of the time-averaged values. Because in the stagnant lid heat is transported by conduction, the temperature at the bottom of the stagnant lid is well approximated by

$$\theta_{lid} = \delta_{lid} Nu, \tag{11}$$

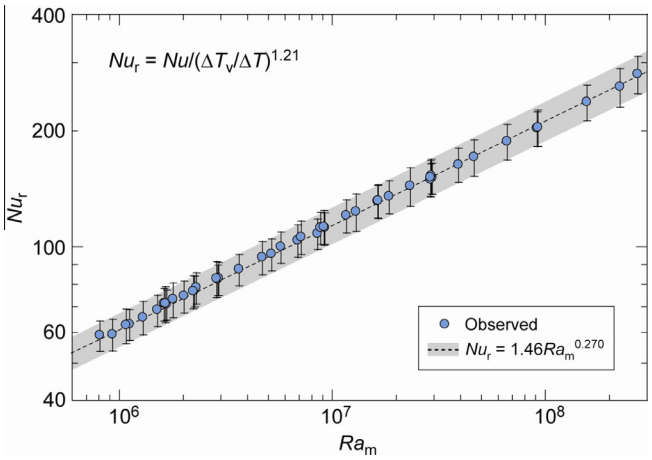

Fig. 5. Reduced Nusselt number as a function of the effective Rayleigh number. The reduced Nusselt number is defined by $Nu_r = Nu/(\Delta T_v/\Delta T)^{1.21}$. Observed values of the Nusselt number are listed in Table 2, and are denoted by the circles. The best fit model to Eq. (10) is indicated by the dashed line, and the shaded band covers one error bar around this best fit model.

A close inspection of Table 2 indicates that δ_{lid} does not monotonically decreases with increasing effective Rayleigh number. Similarly, there is no simple scaling between the surface Rayleigh number and δ_{lid}. Instead, δ_{lid}, depends both on Ra_m and on the amplitude of the viscosity contrast. To model the thickness of the stagnant lid, we have assumed that the sublayer behaves as an isoviscous fluid. In that case, the temperature jump in the top and bottom TBL are equal, *i.e.*, the modeled temperature at the bottom of the lid is

$$\theta_{mod} = 2\theta_m - 1. \quad (12)$$

Assuming that the temperature jump in the bottom TBL is given by Eq. (7), and using the fact that heat is conducted across the lid, the modeled thickness of the stagnant lid is

$$\delta_{mod} = \left[1.0 - 2a_T\left(\frac{\Delta T_v}{\Delta T}\right)\right]/Nu, \quad (13)$$

Using Eq. (10) to calculate the Nusselt number, the thickness of the lid may thus be estimated directly from the input parameters, Ra_0 and $\Delta\eta$. Note that uncertainties in δ_{mod} may be estimated from the uncertainties in Nu and in a_T. Fig. 6 shows that the thickness of the lid modeled with Eq. (13) agrees very well with the measured thickness of the lid (Table 2). This result suggests that the convective sublayer behaves as an isoviscous fluid with a good approximation, as previously pointed out for bottom or volumetrically heated fluids (Davaille and Jaupart, 1993; Moresi and Solomatov, 1995; Grasset and Parmentier, 1998). Assuming that the temperature at the bottom of the lid is given by Eq. (11), our results imply that for a bottom heated fluid the viscosity jump across the sublayer is equal to ~10, which is also the value observed for a volumetrically heated fluid (Davaille and Jaupart, 1993; Grasset and Parmentier, 1998).

4.4. Properties of the convective sublayer

We have further checked whether the convective sublayer behaves as an isoviscous fluid by rescaling the properties of the sublayer with its characteristic temperature and length scales, $(1-\theta_{lid})\Delta T$ and $(1-\delta_{lid})D$. Using these new characteristic quantities, the Rayleigh number, average temperature, and Nusselt number of the sublayer are

$$Ra_{SL} = Ra(1-\theta_{lid})(1-\delta_{lid})^3, \quad (14)$$

$$\theta_{SL} = \frac{(\theta_m - \theta_{lid})}{(1-\theta_{lid})}, \quad (15)$$

and

$$Nu_{SL} = \frac{(1-\delta_{lid})}{(1-\theta_{lid})}Nu. \quad (16)$$

Again, we calculated uncertainties in Ra_{SL}, θ_{SL}, and Nu_{SL} from the uncertainties in θ_m, Nu, and δ_{lid}. The average rescaled temperature slightly decreases with increasing Ra_{SL} (Fig. 7a), but within error bars θ_{SL} mostly remains around 0.5, as one would expect for an isoviscous fluid. Furthermore, Nu_{SL} fit reasonably well along a power law of Ra_{SL} (Fig. 7b),

$$Nu_{SL} = a_{SL}Ra_{SL}^{b_{SL}}, \quad (17)$$

with $a_{SL} = 0.36 \pm 0.04$ and $b_{SL} = 0.31 \pm 0.01$. These values are close to those expected for an isoviscous fluid in 3D-Cartesian geometry, with pre-exponential constant and exponent around 0.27 and 0.32, respectively (e.g., Travis et al., 1990), suggesting again that the convective sublayer behaves nearly as an isoviscous fluid.

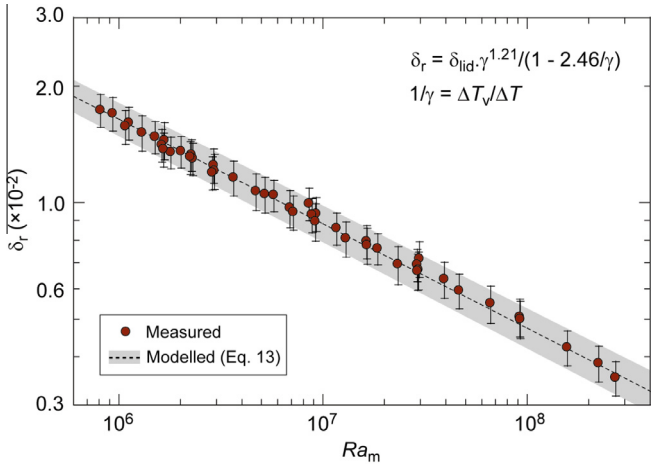

Fig. 6. Reduced thickness of the conductive lid as a function of the effective Rayleigh number. The reduced thickness is defined by $\delta_r = \delta_{lid}[1 - 2.46(\Delta T_v/\Delta T)]/(\Delta T_v/\Delta T)^{1.21}$, where δ_{lid} is the thickness of the stagnant lid. The observed values of the stagnant lid are listed in Table 2 and were measured from the horizontally averaged profile of the vertically advected heat (see main text). The dashed line was constructed by replacing θ_m and Nu in Eq. (13) by their best fit parameterizations (Eqs. (7) and (10), respectively), and the shaded band covers one error bar around this best fit.

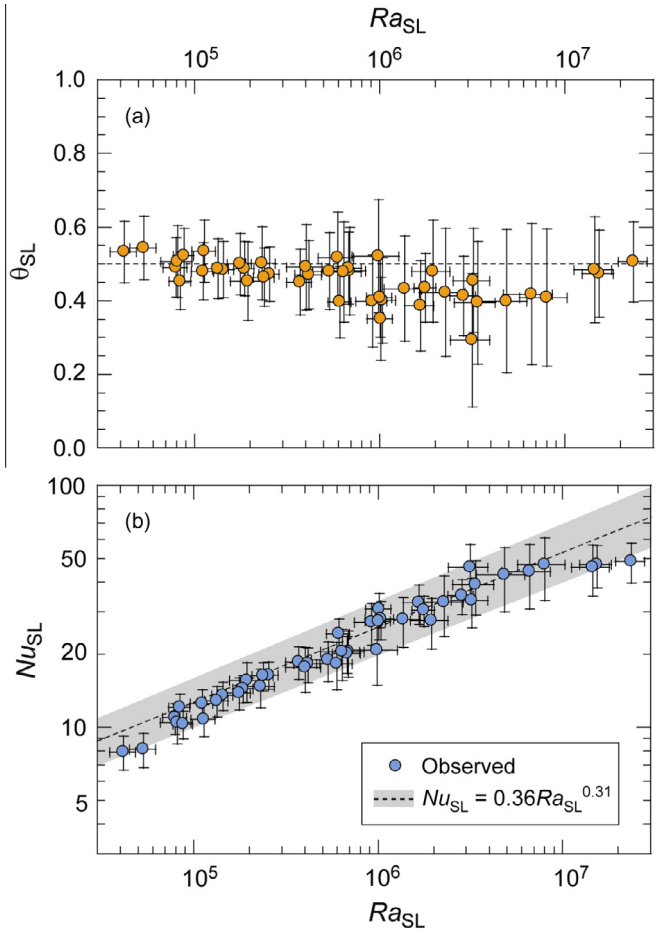

Fig. 7. Properties of the convective sublayer rescaled with the characteristic temperature and length scales of this sublayer. (a) Average temperature, θ_{SL} (Eq. (15)). (b) Nusselt number, Nu_{SL} (Eq. (16)). Results are plotted as a function of the rescaled Rayleigh number, Ra_{SL} (Eq. (14)).

4.5. Comparison with 2D-Cartesian parameterizations

Parameterizations for the average temperature and heat-flux, using the same formalism as the one used in this study, have already been obtained from 2D-Cartesian geometry calculations (*e.g.*, Moresi and Solomatov, 1995; Deschamps and Sotin, 2000) (Table 3). We however observe significant differences between these parameterizations and those derived from our 3D-Cartesian geometry experiments (Figs. 8 and 9). Moresi and Solomatov (1995) parameterized the average temperature as a function of the Rayleigh number (with a very weak dependence), which is not the case in our study. Within the range of Rayleigh number (10^6–10^8) and viscosity contrast (10^6–10^{12}) expected for the outer ice layers of icy moons and dwarf planets, the values predicted by the 2D-Cartesian experiments of Moresi and Solomatov (1995) are however fully consistent (Fig. 8). Differences between our 3D-Cartesian parameterization and that from Deschamps and Sotin (2000), which also does not account for variations of the temperature with the Rayleigh number, are larger. More importantly, we observe substantial differences in the convective heat flux, with 3D-Cartesian parameterizations predicting a better heat transfer than 2D-Cartesian parameterizations (Fig. 9a). Compared to our 3D-Cartesian calculations, the experiments of Moresi and Solomatov (1995) predict a weaker dependence on both the Rayleigh number and the thermal viscosity contrast (Table 3). Experiments from Deschamps and Sotin (2000) predict a slightly weaker dependence on the Rayleigh number, but a stronger dependence on the thermal viscosity contrast. As a result, in the range of Rayleigh number and thermal viscosity contrasts expected for the outer ice layers of icy moons, the heat flux predicted by our 3D-Cartesian parameterization is larger than the heat flux predicted Moresi and Solomatov (1995) by up to 40%. Again, larger differences, between 25% and 50% are observed between our results and those of Deschamps and Sotin (2000).

Because the 2D-Cartesian heat flux parameterization of Moresi and Solomatov (1995) was deduced from steady calculations only, the comparison between this scaling and our 3D-Cartesian heat flux parameterization may be biased. Dumoulin et al. (1999) pointed out that time-dependent calculations predict a different heat flux parameterization than steady state calculations. For time-dependent cases, they found that a heat flux parameterization with exponents of the Rayleigh number and non-dimensional viscous temperature scale equal to 1/3 and 4/3 (Table 3) explains their data well. Solomatov and Moresi (2000) found a similar parameterization for volumetrically heated 2D-Cartesian boxes, and in its Cartesian limit, the parameterization obtained by Reese et al. (2005) from spherical calculations has exponents of the Rayleigh number and viscous temperature scale equal again to 1/3 and 4/3, respectively, but a slightly larger value of the pre-exponential constant (Table 3).

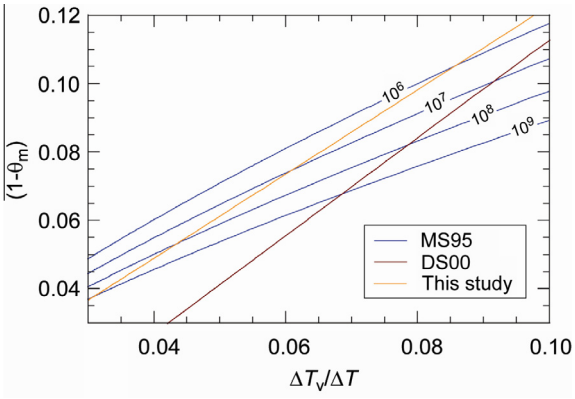

Fig. 8. Comparison between parameterizations for the temperature jump across the bottom TBL built from 2D-Cartesian and 3D-Cartesian experiments. The blue lines are from Moresi and Solomatov (1995) for Rayleigh number between 10^6 and 10^9 (labels on curves), the dark red line from Deschamps and Sotin (2000), and the orange line is from this study. Results are shown as a function of the viscous temperature scale $\Delta T_v/\Delta T$.

Compared to our 3D-Cartesian heat flux parameterization, the 2D-Cartesian parameterization of Dumoulin et al. (1999) predicts value of the Nusselt number lower by 20–40% in the range of Rayleigh number relevant to icy moons (typically, 10^6–10^8) (Fig. 9b). Because the Rayleigh exponent used in this parameterization is larger than in our 3D-Cartesian scaling, this difference decreases with increasing Rayleigh number. On the contrary, the discrepancies between the two parameterizations increases with increasing viscosity contrast. For a Rayleigh number of 10^6, the Nusselt number predicted by the parameterization of Reese et al. (2005) is still lower than that obtained by our parameterization by 20–30%, depending on the viscosity contrast, but for Rayleigh number around 10^8 the two scalings lead to similar amount of heat transfer, and for a Rayleigh number of 10^9 the parameterization of Reese et al. (2005) now predicts a more efficient heat transfer than our parameterization.

Dumoulin et al. (1999) pointed out that the parameterization with a 1/3 Rayleigh exponent is valid only for cases in a chaotic regime, in which secondary instabilities rapidly grow in the TBL, implying a larger heat flux. This chaotic regime appears for large values of the effective Rayleigh number (typically, $>10^8$). Other time-dependent cases, in quasi-stationary state and with effective Rayleigh number around 5.0×10^7 and less, are not explained by the 1/3 Rayleigh exponent parameterization (Fig. 10). The parameterization of Deschamps and Sotin (2000), on another hand, explains both steady and time-dependent (but not chaotic) cases (blue crosses in Fig. 10), including the data of Dumoulin et al.

Table 3
Comparison between 2D- and 3D-Cartesian parameterizations.

References	θ_m	Nu
Moresi and Solomatov (1995)	$(1-\theta_m) = 1.1\left(\frac{\Delta T_v}{\Delta T}\right)^{0.73} Ra_m^{-0.04}$	$Nu = 1.89 Ra_m^{0.2}\left(\frac{\Delta T_v}{\Delta T}\right)^{1.02}$
Deschamps and Sotin (2000)	$(1-\theta_m) = 1.43\left(\frac{\Delta T_v}{\Delta T}\right) - 0.03$	$Nu = 3.8 Ra_m^{0.258}\left(\frac{\Delta T_v}{\Delta T}\right)^{1.63}$
Dumoulin et al. (1999)		$Nu = 0.52 Ra_m^{1/3}\left(\frac{\Delta T_v}{\Delta T}\right)^{4/3}$
Reese et al. (2005)		$Nu = 0.67 Ra_m^{1/3}\left(\frac{\Delta T_v}{\Delta T}\right)^{4/3}$
This study	$(1-\theta_m) = 1.23\left(\frac{\Delta T_v}{\Delta T}\right)$	$Nu = 1.46 Ra_m^{0.270}\left(\frac{\Delta T_v}{\Delta T}\right)^{1.21}$

Non-dimensional temperature and Nusselt number are parameterized as a function of the non-dimensional temperature scale, $\Delta T_v/\Delta T$, which is equal to the inverse of the logarithmic thermal viscosity contrast $\gamma = \ln(\Delta\eta)$, and of the Rayleigh number of the well-mixed interior, Ra_m. Note that the parameterization from Dumoulin et al. (1999) was built from time-dependent experiments in boxes with aspect ratio 4. The parameterization of Reese et al. (2005) is the Cartesian limit of a scaling built from experiments in spherical geometry.

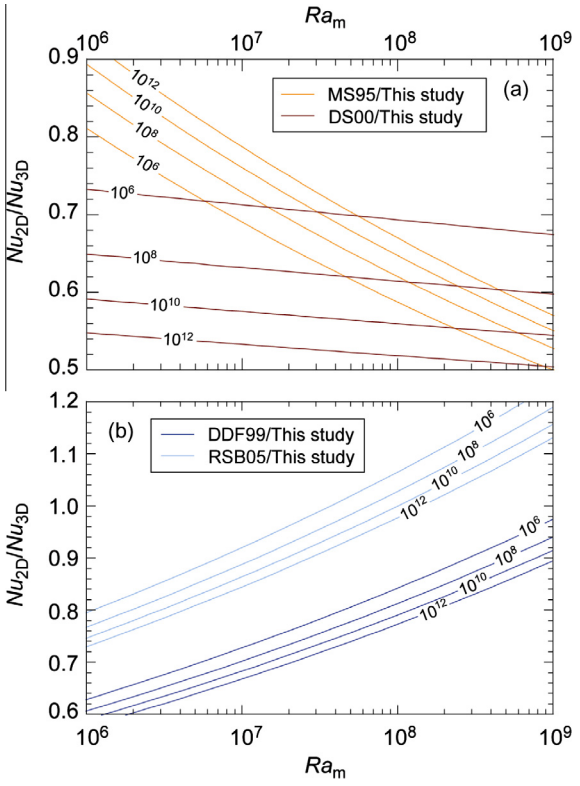

Fig. 9. Ratio between the Nusselt number predicted from 2D-Cartesian and 3D-Cartesian (this study) parameterizations. Results are shown as a function of the Rayleigh number, and for values of the thermal viscosity ratio between 10^6 and 10^{12} (labels on curves). (a) Orange curves are from Moresi and Solomatov (1995), and dark red curves from Deschamps and Sotin (2000). (b) Dark blue curves are from the time-dependent scaling from Dumoulin et al. (1999), and light blue curves are from the Cartesian limit of the spherical geometry parameterization of Reese et al. (2005).

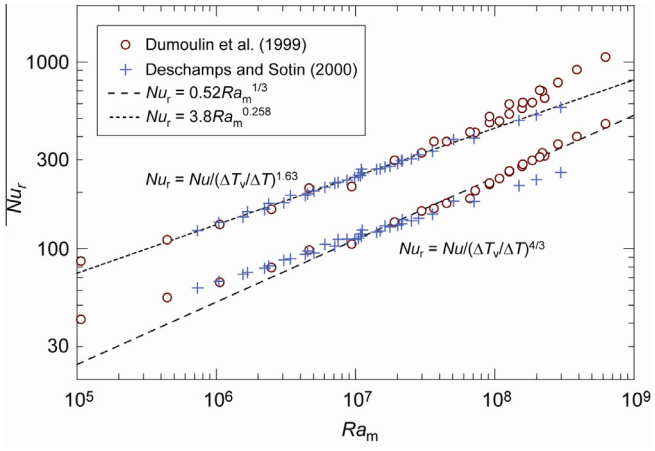

Fig. 10. Reduced Nusselt number as a function of the effective Rayleigh number. Dark red rings are the time-dependent data of Dumoulin et al. (1999) for Newtonian cases with viscosity depending on temperature only. Blue crosses are all data from Deschamps and Sotin (2000) plus additional cases at high (>10^8) Rayleigh number. Two reduced Nusselt number are considered, $Nu_r = Nu/(\Delta T_v/\Delta T)^{4/3}$ (dashed line and bottom series of points), as suggested by Dumoulin et al. (1999), and $Nu_r = Nu/(\Delta T_v/\Delta T)^{1.63}$ (dotted line and top series of points), as found by Deschamps and Sotin (2000). (For interpretation of the references to color in this figure legend, the reader is referred to the web version of this article.)

(1999) up to effective Rayleigh number around 10^8. Additional 2D-Cartesian quasi-stationary calculations indicate that it explains cases with Rayleigh number up to at least 3.0×10^8. A possible explanation for the chaotic regime is that the appearance of stagnant lid convection may depend on both the viscosity contrast and the Rayleigh number (Deschamps and Sotin, 2000). For values of the Rayleigh number larger than a critical value, which increases with the viscosity contrast, convection operates in an intermediate regime between stagnant lid and isoviscous convection.

Whatever the nature of the chaotic regime observed by Dumoulin et al. (1999), this regime implies the development of instabilities at very short time scales, which may be too fast compared to the growth of instabilities within ice layers of icy moons and dwarf planets. Time-dependent, quasi-stationary flows predict lower heat flux (thus, according to Eq. (4), longer time for the growth of instabilities) and may be better suited in these cases. It is also worth noting that the heat flux may be affected by interactions between the top and bottom TBLs. The 1/3 value of the Rayleigh number exponent in heat flux parameterizations is an asymptotic value, which assumes that TBLs do not interact with one another and that heat is only driven by the growth of instabilities in these layers. In practice, however, hot plumes and cold downwellings interact with the bottom and top TBL, respectively, thus perturbing the growth of instabilities (*e.g.*, Labrosse, 2002), and potentially affecting the value of the Rayleigh number exponent.

5. Application to the outer ice I shells of icy moons

The parameterizations we inferred may be used to model the cooling of icy moons and dwarf planets of the outer solar system. A possible radial structure of the largest icy moons (Callisto, Ganymede, and Titan) consists of a core of silicate, surrounded by a layer of high pressure ices, and an outer ice I shell. If heat transfer in this shell is not efficient enough, a subsurface ocean of water and volatiles may subsist in between the high pressure ice and ice I layers. The moment of inertia of Ganymede indicates that its core have further differentiated in an metallic core and a silicate shell. By contrast, the moment of inertia of Callisto suggests that this satellite is not fully differentiated, *i.e.*, its core consists in a mixture of ice and silicates. Based on their average density, medium size bodies (including Europa and Pluto) have a relatively large core, with radius around 75% and more of the total radius. The layer of ice may reach 250 km at most, and in these conditions, the gravity acceleration does not allow the presence of a high pressure ice layer above the silicate layer. However, a subsurface ocean may still be present beneath the outer ice I shell, directly overlying the silicate core. Subsurface oceans were first proposed to exist in icy moons, as a consequence of the phase diagram of water (Lewis, 1971). They may however be a more general feature of satellites and dwarf planets composed of ices and rocks (Hussmann et al., 2006). A subsurface ocean may also exist in Ceres, provided that this asteroid has lost little water during its history (McCord and Sotin, 2005). The exact thickness of the ocean is likely controlled by the presence of anti-freeze compounds (including ammonia and methanol), whose effect is to decrease the liquidus of water at a given pressure. Even in small concentrations (3 wt% or less), ammonia can induce a 50–100 km thick subsurface ocean (Grasset et al., 2000; Deschamps and Sotin, 2001). More recently, Deschamps et al. (2010a) showed that the combination of 4 wt% methanol and 1 wt% ammonia would maintain a 90 km thick ocean in Titan. Furthermore, due to periodic switches between conductive and convective modes of heat transfer in the outer ice I shell, the thickness of the ocean may oscillate by a few kilometers (Mitri and Showman, 2008). An important consequence of the decrease in the temperature is an increase in the bulk viscosity of the outer ice I shell, which in turn strongly reduces the vigor of convection and the heat transfer in this shell. This further opposes the crystallization of the ocean and the cooling of the planetary interior.

Similarly, tidal heating, if active, is likely slowing down the crystallization of the ocean and the cooling of the body (*e.g.*, Tobie et al., 2006).

A detailed study of the thermal evolution of large icy moons and dwarf planets is beyond the scope of this paper. Application of the parameterizations inferred in the previous section to the heat transfer through the outer ice I layer however leads to important qualitative conclusions, which we discuss here. An interesting effect, when volatiles are present in the primordial ocean, is that the Rayleigh number of the outer ice I shell increases with the thickness of this layer up to a maximum value, and then starts decreasing again (Grasset and Sotin, 1996; Deschamps and Sotin, 2001; Deschamps et al., 2010a). This effect is a consequence of the phase diagram of the water + volatile system. The temperature at the bottom of the ice I layer, which is by definition equal to the temperature of crystallization at this depth, decreases with increasing thickness of the ice layer. As a consequence, the temperature of the well-mixed interior decreases, and the viscosity increases, which compensate the increase of Rayleigh number due to the thickening of the ice layer. For pure water, the thickening always dominates the increase in viscosity, *i.e.*, the Rayleigh number always increases with increasing thickness of ice I. The presence of volatiles, however, further decreases the temperature of crystallization of the ocean, which further increases the effective viscosity. As a result, the Rayleigh number decreases with increasing weight fraction of volatile. Given the volume fraction of volatile, there is a thickness for which the increase in Rayleigh number due to the thickening is fully balanced by the increase in viscosity. For thicker layers, the Rayleigh number decreases with increasing thickness. If the ice I layer is too thick, the Rayleigh number of the ice I layer is lower than the critical Rayleigh number for the onset of convection, *i.e.*, the ice I layer is stable. Here, we used our scalings to calculate the heat flux and the thickness of stagnant lid as a function of the ice I layer, and the critical thickness of ice I at the convection shut-off for four selected bodies, Europa, Ganymede, Titan, and Pluto (physical properties of these bodies are listed in Table 4).

Details of the calculations can be found in Deschamps and Sotin (2001). We first calculate the temperature at the bottom of the ice I layer, T_{bot}, as a function of the thickness of the ice I layer, D_{ice}, and of the initial weight fraction of volatile in the ocean. The bottom temperature derives from the phase diagram of the mix of water and volatiles, the pressure being deduced from D_{ice}. Here, we used the phase diagram of the system water + ammonia, because it is better known (Sotin et al., 1997) than that of other systems. The presence of methanol, which in the case of Titan may be 4 times more abundant (in weight fraction) than ammonia, can be taken into account noting that the effect of 5 wt% methanol on the dynamics of the ice I layer is equivalent to that of 3 wt% ammonia (Deschamps et al., 2010a). For instance, the presence of 1 wt% ammonia and 4 wt% methanol may be modeled assuming a primordial ocean containing 3.5 wt% ammonia. For large objects (here, Ganymede and Titan) a high pressure ice layer also crystallizes between the core and the bottom of the ocean. Assuming that the ocean is adiabatic, and using the phase diagram of the high pressure ices, we calculate the depth of the transition between the ocean and the high pressure ice, from which we deduce the thickness of the remaining ocean. For smaller bodies (here Europa and Pluto), high pressure ices do not form beneath the ocean, and the bottom of the ocean is simply given by the radius of the core). Note that as long as the fraction of ammonia is smaller than that at the eutectic composition (which is equal to 32.2 wt% for the water + ammonia system), only water crystallizes, leaving volatiles in the ocean. Thus, as the ice I thickens, the fraction of ammonia in the remaining ocean increases, and the bottom temperature should be updated according to this increase. We addressed this problem using an iterative Newton–Raphson method.

The viscosity of ice I is strongly temperature dependent and is well described by

$$\eta(T) = \eta_{ref} \exp\left[\frac{E}{RT_{ref}}\left(\frac{T_{ref}}{T} - 1\right)\right], \tag{18}$$

where E is the activation energy of ice I, R is the ideal gas constant, and η_{ref} is the reference viscosity at temperature T_{ref}. Here, we used $\eta_{ref} = 5.0 \times 10^{13}$ Pas (Deschamps and Sotin, 2001), a value derived from the viscosity of pure water ice close to the melting point and at strain rate around 10^{-11} s^{-1} (Gerrard et al., 1952). A potential flaw in our modeling is that our numerical experiments are built for a Newtonian flow (*i.e.*, the stress exponent in the stress/strain relationship is equal to 1). By contrast, at icy moons conditions, the ice flow is likely non-Newtonian (*e.g.*, Goodman et al., 1981). Interestingly, Dumoulin et al. (1999) have shown that Newtonian scaling laws may capture non-Newtonian behaviors by prescribing smaller values of the activation energy. Furthermore, varying the activation energy in the range 30–90 kJ/mol previous studies (Deschamps and Sotin, 2001; Deschamps et al., 2010a) have found that the influence of activation energy on the ice I shell properties is small compared to that of the presence of volatiles. The error induced by using Newtonian scalings instead of non-Newtonian scalings may thus be accounted for by enlarging the uncertainty on the activation energy of ice I, and because varying this activation energy have moderate effects, the errors induced by the use of Newtonian scalings is limited. Here, we use $E = 60$ kJ/mol, which is consistent with experimental data (Durham et al., 1997; Goldsby and Kohlstedt, 2001; Durham and Stern, 2001).

Given the temperature at the bottom of the ice I layer and the viscosity law, the temperature of the well-mixed interior T_m can be calculated by rescaling Eq. (7),

$$T_m = T_{bot} - 1.23\Delta T_v. \tag{19}$$

Following Eq. (18), the viscous temperature scale (Eq. (6)) is given by

$$\Delta T_v = \frac{RT_m^2}{E}. \tag{20}$$

Inserting Eq. (20) in Eq. (19), T_m satisfies a degree 2 polynomial, of which it is the positive solution.

The effective Rayleigh number of the ice I layer, calculated with the viscosity at temperature T_m, is

$$Ra_{ice} = \frac{\alpha_I \rho_I g \Delta T_{ice} D_{ice}^3}{\eta(T_m)\kappa_I}, \tag{21}$$

Table 4
Properties of selected planetary bodies.

Body	R (km)	ρ (kg/m^3)	r_c (km)	T_{surf} (K)	g (m/s^2)
Europa	1561	3020	1400	102	1.31
Ganymede	2631	1940	1700	110	1.43
Titan	2575	1880	1800	94	1.35
Pluto	1153	2000	900	44	0.66

Listed parameters are the total radius R, the average density ρ, the estimated radius of the silicate mantle or core r_c, and the surface temperature T_{surf}, the surface gravity acceleration g.

where $\Delta T_{ice} = (T_{bot} - T_{surf})$ is the temperature jump across the ice I layer, g the surface gravity acceleration, and α_I, ρ_I, κ_I the thermal expansion, density, and thermal diffusivity of ice I (Table 5). When Ra_{ice} becomes smaller than a critical value, the ice I layer stops convecting. For stagnant lid regime, the critical Rayleigh number depends on the viscous temperature scale, a good approximation being given by Stengel et al. (1982). Their experiments and calculations indicate that the critical surface Rayleigh number is well explained by

$$Ra_{crit,surf} = 20.9\gamma^4 \ \exp(-\gamma), \tag{22}$$

where $\gamma = \Delta T/\Delta T_v$. Following Eq. (3), the critical effective Rayleigh number is

$$Ra_{crit} = 20.9\gamma^4 \exp\left[-\frac{(T_{bot} - T_m)}{\Delta T_v}\right] \tag{23}$$

which, using Eq. (19) and $\gamma = \Delta T/\Delta T_v$, reduces to

$$Ra_{crit} = 6.1\left(\frac{\Delta T}{\Delta T_v}\right)^4. \tag{24}$$

We obtained the convective heat flux through the ice I layer by rescaling Eq. (10) with the conductive heat flux Φ_c across the ice I layer, leading to

$$\Phi_{ice} = 1.46\ Ra_{ice}^{0.270}\left(\frac{\Delta T_v}{\Delta T_{ice}}\right)^{1.21}\Phi_c, \tag{25}$$

where the viscous temperature scale ΔT_v is given by Eq. (20), $\Phi_c = k_I \Delta T_{ice}/D_{ice}$, and k_I the thermal conductivity of ice I. After convection stopped, the heat flux through the ice I layer is of course given by the conductive heat flux Φ_c.

Finally, it is interesting to calculate the thickness of the stagnant lid at the top of the ice I layer because it is a good proxy for the lithospheric strength. The thicker the lid, the stronger the lithosphere, thus reducing the surface tectonic activity. The thickness of the lid may be obtained by rescaling Eq. (13) following

$$d_{lid} = \frac{\Delta T_{ice} - 2.46\Delta T_v}{\Phi_{ice}}, \tag{26}$$

where the convective heat flux Φ_{ice} is given by Eq. (25).

Fig. 11 plots the Rayleigh number (Eq. (21)), the convective heat flux (Eq. (25)) and the thickness of the stagnant lid (Eq. (26)) as a function of the thickness of the ice I layer, D_{ice}, for Europa, Ganymede, Titan, and Pluto, and for two values of the weight fraction of ammonia. As expected, the Rayleigh number first increases with D_{ice}, then reaches a maximum, and decreases until it becomes smaller than the critical Rayleigh number for the onset of convection (Fig. 11a and b). The convective heat flux (Fig. 11c and d) monotonically decreases with increasing D_{ice}. This is a combined effect of the variations of the Nusselt number, which follow those of the Rayleigh, and of the conductive heat flux Φ_c, which monotonically decreases with D_{ice}. Overall, the amount of heat that can be extracted from the interior decreases as the ice I layer thickens. Heat transfer is further reduced when the ice I layer becomes too thick and convection shuts off. Thus, if the radiogenic heat is too large, or if additional heat is produced by tidal heating, heat may not be fully transported from the bottom of the ice I layer to its surface, and the crystallization of this layer may stops. The thickness of the stagnant lid, d_{lid}, is inversely proportional to the heat flux through the ice layer (Eq. (26)), and thus increases with D_{ice} (note that this increase is slightly moderated by the decrease in the temperature ΔT_{ice} as the ice layer thickens) (Fig. 11e and f). It is interesting to note that after the Rayleigh number has reached its maximum value, d_{lid} sharply increases. Assuming that the thickness of the stagnant lid is a good proxy for the lithospheric strength, these results suggest that the surface tectonic activity should reduce with thickening of the ice I layer.

Unsurprisingly, increasing the weight fraction of volatile strongly reduces the vigor of convection, and restricts the range of D_{ice} in which convection can operate. For $x_{NH3} = 3.5\%$, convection may operate in the ice I layers of Europa, Ganymede, and Titan if they are thinner than 130–140 km, but for $x_{NH3} = 8.5\%$ convection stops as soon as the thickness of the ice I layer reaches 90 km. This effect is further quantified in Fig. 12a. For pure water, complete crystallization of the ocean may be achieved. The thickness of ice I at the convection shut-off then decreases with the weight fraction of volatile (here ammonia). For a given thickness of ice I, an increase in the weight fraction of volatile in the ocean also induces substantial decrease in the heat flux, due the decrease in Rayleigh number (Fig. 11c and d). If, for instance, $D_{ice} = 50$ km, the heat flux through the ice I layers of Europa, Ganymede and Titan drops from about 30 mW/m^2 for $x_{NH3} = 3.5\%$ to about 20 mW/m^2 for $x_{NH3} = 8.5\%$. Due to the decreases in the vigor of convection, the thickness of the stagnant lid also increases with increasing weight fraction of volatiles. For $D_{ice} = 50$ km, the thickness of the stagnant lid for Europa, Ganymede and Titan is around 12 km for $x_{NH3} = 3.5\%$, and 18 km for $x_{NH3} = 8.5\%$. An interesting consequence of this result is that less tectonic features may be generated at the surface bodies having an ocean rich in volatiles. This may explain the lack of tectonic features at the surface of Titan (Moore and Pappalardo, 2001).

Figs. 11 and 12 point out major differences between the properties of Pluto's ice I layer and those of the three others selected bodies. Convection in Pluto's outer ice I layer is more vigorous and can be maintained for thicker layers than in Europa, Ganymede, and Titan (Fig. 11a and b). For Pluto, and taking $x_{NH3} = 3.5\%$, the maximum Rayleigh number is reached for $D_{ice} = 135$ km, whereas for Europa, Ganymede, and Titan it is reached around $D_{ice} = 90$ km. Still for $x_{NH3} = 3.5\%$, convection in the ice I layer of Europa, Ganymede, and Titan stops if this layer is thicker than about 130–140 km, but it is still at work in the ice I layer of Pluto up to $D_{ice} = 200$ km. Fig. 12a clearly shows that for a given initial weight fraction of ammonia, the thickness of the outer ice I layer of Pluto at the convection shut-off is larger than that of Europa, Ganymede, and Titan. From this it follows that heat transfer is more efficient in Pluto, and that it is less affected by the thickening of the ice I (Fig. 11c and d). These differences can be explained by the differences in gravity acceleration and surface temperature (Table 4). Due to Pluto's smaller acceleration of gravity, the pressure increases with depth at a smaller rate than in other bodies. For a given thickness of ice I, the phase diagram of water implies that the temperature at the bottom of ice I is larger in Pluto than in other bodies. This in turn induces a larger temperature of the well mixed interior, and therefore a smaller bulk viscosity in Pluto than in Europa, Ganymede, and Titan. The thickness of the stagnant lid in Pluto's ice I layer also strongly

Table 5
Ice I properties.

Parameter	Symbol	Unit	Value
Density	ρ_I	kg/m^3	917
Thermal conductivity	k_I	W/m/K	2.6
Thermal expansion	α_I	1/K	1.56×10^{-4}
Thermal diffusivity	κ_I	m^2/s	1.47×10^{-4}
Latent heat of fusion	L_I	kJ/kg	284
Reference bulk viscosity	η_{ref}	Pas	5.0×10^{13}
Activation energy	E_a	kJ/mol	60

All data are from Hobbs (1974), except the reference viscosity, which is deduced from the viscosity of ice close to the melting point (Gerrard et al., 1952), and the activation energy, which is deduced from ice flow experiments under different regimes (Durham et al., 1997; Goldsby and Kohlstedt, 2001; Durham and Stern, 2001).

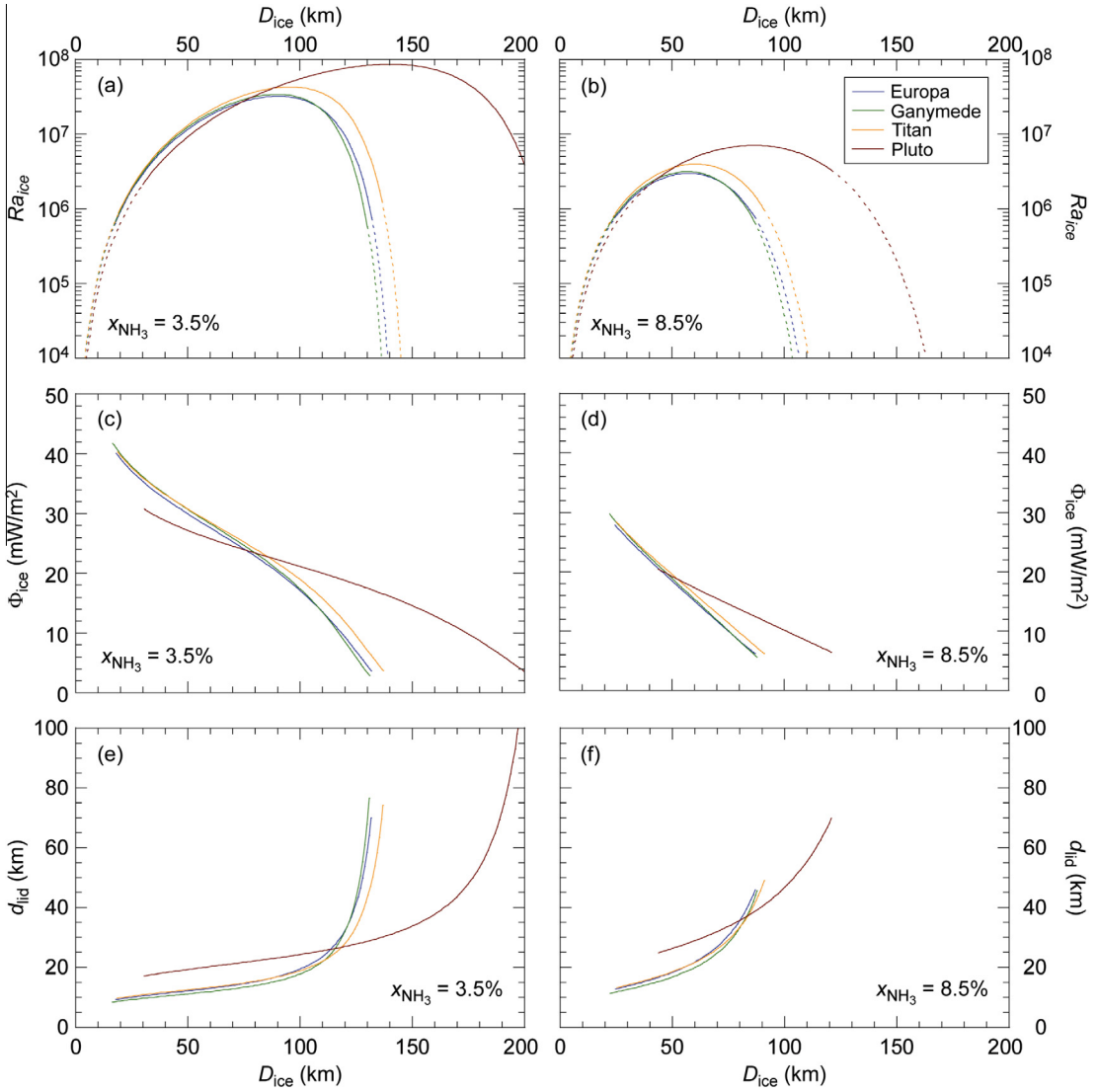

Fig. 11. (a) Rayleigh number of the ice I layer (Eq. (21)) of Europa, Ganymede, Titan, and Pluto (see legend) for an initial fraction of ammonia x_{NH3} = 3.5%. The dashed part of the curves denotes Rayleigh number smaller than the critical Rayleigh number (Eq. (24)). (b) Same as panel (a), but for an initial fraction of ammonia x_{NH3} = 8.5%. (c) Convective heat flux through the ice I layer (Eq. (25)) of Europa, Ganymede, Titan, and Pluto (see legend) for an initial fraction of ammonia x_{NH3} = 3.5%. (d) Same as panel (c), but for an initial fraction of ammonia x_{NH3} = 8.5%. (e) Thickness of the stagnant lid at the top of the ice I layer (Eq. (26)) of Europa, Ganymede, Titan, and Pluto (see legend) for an initial fraction of ammonia x_{NH3} = 3.5%. (f) Same as panel (e), but for an initial fraction of ammonia x_{NH3} = 8.5%. In all panels, results are presented as a function of the total thickness of ice I, D_{ice}. In panels (c–f), results are shown only in the range of D_{ice} for which the ice I layer is convecting.

differs from those in other bodies (Fig. 11e and f). These differences have two origins, the smaller gravity acceleration at Pluto and its smaller surface temperature (Table 4). First, a smaller gravity acceleration induces larger effective Rayleigh number (due to the decrease in bulk viscosity), which delays the sharp increase in the thickness of the stagnant lid. Second, a decrease in the surface temperature increases the temperature jump ΔT_{ice}. For a given value of D_{ice}, a smaller surface temperature therefore results in an increase in d_{lid} (Eq. (26)). An interesting consequence is that tectonic activity at the surface of Pluto, where T_{surf} = 44 K, should be reduced compared to that at the surface of Europa, where T_{surf} = 102 K.

The thickness of the ice I layer at the convection shut-off may be understood as an upper bound estimate for the current thickness of this layer. This assumes that the heat transfer through the outer ice I shell is large enough to allow the crystallization of the ocean as long as this layer is animated by convection. In some cases, *e.g.*, if the ice layer is thin enough, heat conduction through the ice I layer may still be efficient enough to transport radiogenic heat from the core and drive the crystallization of the ocean. A precise estimate of the current thickness of the outer ice I layer requires a full modeling of the thermal evolution of icy moons. In the case of Titan, and using parameterizations for isoviscous fluids, Grasset and Sotin (1996) found that the a pure water ocean may crystallize in 300 Myr. For an ocean with 15 wt% ammonia, they found that the thickness of the outer ice I layer reaches a limit of about 50 km. Using a more detailed modeling, which accounts for tidal heating and parameterizations for 2D-Cartesian stagnant lid convection, Tobie et al. (2006) reached similar conclusions. The thickness of ice I at the convection shut-off we calculated (Fig. 12a) are in good agreement with this limit, keeping in mind that in the calculations of Grasset and Sotin (1996) and Tobie et al. (2006) the fraction of ammonia in the ocean is kept constant throughout the evolution, whereas in our calculations this fraction increases as the ice I thickens. For Titan, our calculations indicate that the fraction of ammonia in the remaining ocean reaches 15 wt% for

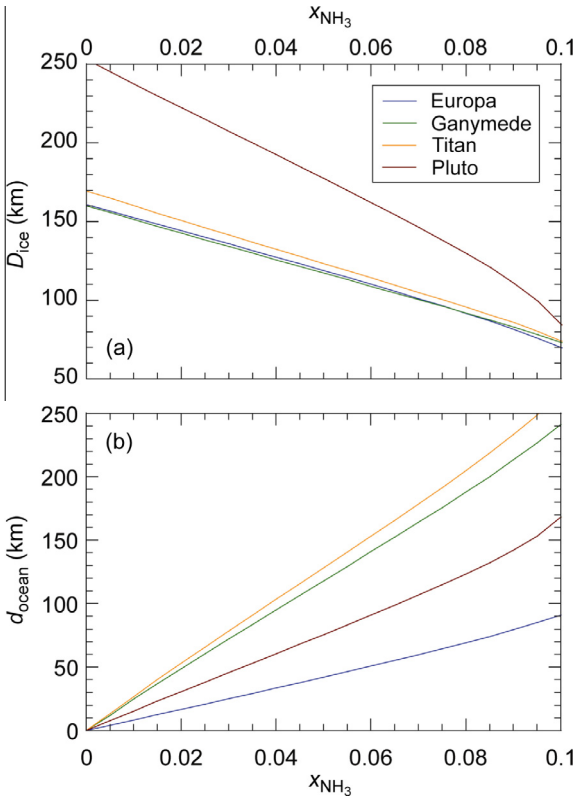

Fig. 12. (a) Thickness of the ice I layer at the convection shut-off. (b) Thickness of the remaining ocean at the convection shut-off. Results are shown as a function of the initial weight fraction of ammonia in the ocean x_{NH3}.

an initial fraction of ammonia equal to about 11 wt%, in which case the thickness of ice I layer at the convection shut-off is about 60 km. This suggests that the thickness of ice I at the convection shut-off is indeed a good estimate for the upper bound thickness of the present ice I layer. Again, it is important to note that thicker ice I layers may crystallize as gravity acceleration decreases (Fig. 12a). Whatever the initial weight fraction of ammonia in the ocean, the thickness of ice I at the convection shut-off is larger in Pluto than in Europa, Ganymede, and Titan. Finally, a lower bound for the thickness of the remaining ocean can be deduced from the upper bound of the ice I thickness (Fig. 12b). This thickness depends of course on the radius of the silicate core, and on the thickness of the high pressure ice layer, if present.

6. Conclusion and perspectives

A good knowledge of the properties of stagnant lid convection, including average temperature of the well-mixed interior, transported heat flux, and thickness of the stagnant lid, is essential for a more accurate modeling of the heat transfer through the ice shells of icy moons and dwarf planets. In this article, we derived appropriate parameterizations for the temperature, heat flux, and thickness of the stagnant lid based on the effective Rayleigh number and on a viscous temperature scale. Because the outer ice shells of icy moons and dwarf planets have small curvatures (with ratio between inner and outer radii around $f = 0.8$ or larger), convection in these layers may be approximated with 3D-Cartesian calculations with a good accuracy, and the parameterizations we obtained may be used to estimate their properties, including their ability to transfer heat (with differences in heat flux around 10–20%, depending on the curvature of the icy shell, see below). Coupled with the phase diagrams of the water + volatile systems, these parameterizations allow quantifying the influence of volatiles on the crystallization of the primordial ocean of these bodies. Our calculations further indicate that the gravity acceleration, by controlling the pressure at the bottom of the ice I layer, has an substantial influence on the crystallization of the ocean. Thicker ice I layers may be achieved in bodies such has Pluto, whose gravity acceleration is small (around 0.7 m/s^2), that in bodies like Europa, Ganymede, and Titan, whose gravity acceleration is larger (around 1.3 m/s^2). Furthermore, the surface temperature partially controls the thickness of the stagnant lid, and therefore the lithospheric strength. Decrease in the surface temperature result in a thicker stagnant lid, thus in a stronger lithosphere. This implies that fewer tectonic activity may be present at the surface of Pluto than at the surface of Europa. Note that if the surface of Pluto is not made of pure water ice but also includes softer compounds, deformation may still be present at its surface.

More detailed quantitative estimates for the present radial structures of icy moons and dwarf planets require modeling the full thermal evolution of icy moons (*e.g.*, Grasset and Sotin, 1996; Tobie et al., 2006). Coupled to parameterizations obtained for pure internal heating (*e.g.*, Grasset and Parmentier, 1998; Deschamps et al., 2012), which may be used to model the cooling of the silicate cores, the parameterizations obtained in the present study may provide refined models for the thermal evolution and present radial structure of icy moons. More accurate models should also account for additional sources of heating related to tidal dissipation within the ice layers. If the convective heat flux is not large enough to transport the cumulated heat from radiogenic and tidal origins, crystallization of the ocean will stop. Furthermore, if tidal heat is generated within the ice I layer, the parameterizations for heat flux and temperature obtained for purely bottom heated fluid may not be valid. For an isoviscous fluid, numerical studies in various geometries (*e.g.*, Travis and Olson, 1994; Sotin and Labrosse, 1999; Moore, 2008; Deschamps et al., 2010b) have shown that the flow pattern and heat transfer are strongly modified as the amount of internal heating increases. Tidal dissipation is important for satellites that have not reached a synchronous spin (which may have been the case of Europa, Ganymede and Titan early in their histories), and for large satellites that are moving on eccentric orbits close to their parent planets. The calculations of Tobie et al. (2005) suggest that the rate of internal heating within the ice I layer of a generic satellite vary laterally. Typically, the average value of tidal heating is around 10^{-10} W/kg, corresponding to non-dimensional rate of internal heating around 5. For an isoviscous fluid with homogeneous internal heating, such amount of internal heating has a moderate effect of the convection pattern (*e.g.*, Travis and Olson, 1994; Sotin and Labrosse, 1999; Deschamps et al., 2010b). The effect of heterogeneous distribution of tidal heating on convection pattern and heat transfer remain to be investigated.

Stagnant lid convection in spherical geometry will be useful to refine the modeling of the evolution of ice shells (including the high-pressure ice layers, if present), and the heat transfer through them. Preliminary calculations in spherical geometry indicate that the Nusselt number is larger than in 3D-cartesian geometry by 8% for a ratio between inner and outer radii $f = 0.9$, and 16% for $f = 0.8$. Our scaling may further be used as an end-member case (zero curvature) for parameterizations in spherical geometry. Furthermore, numerical experiments of isoviscous thermal convection in spherical geometry pointed out that the average temperature decreases with increasing curvature (*e.g.*, Shahnas et al., 2008; Deschamps et al., 2010b), which may influence the development of the stagnant lid regime. Since the temperature jump in the top thermal boundary layer decreases with increasing curvature, generating a rigid lid at the top of the system may be more difficult as the curvature increases. The stagnant lid regime may thus appear at larger viscosity ratios as the curvature increases (*i.e.*, as the thickness of

the ice I layer increases). Additional mineral physics experiments are also needed to better constrain the phase diagrams of water + volatiles systems. In particular, since it has been spectroscopically observed in more than ten comets with abundances (relative to water) up to 7 wt% (Mumma and Charnley, 2011), methanol may enter the composition of the primordial ocean of icy moons in substantial amounts. The combination of models of stagnant lid convection in spherical geometry and of new experimental data on the phase diagram of the water + volatile systems will likely result in more accurate modeling of the structure and thermal evolution of large icy moons and dwarf planets.

Acknowledgments

We are grateful to Bill McKinnon for his constructive review and to the editor (Mark Jellinek) for his comments, which both helped improving a first version of this article. The research presented in this article was supported by the National Science Council of Taiwan (NSC) under Grant 101-2116-M-001-001-MY3. The computational effort was shared between the cluster of ETH Zürich (brutus), and the cluster of the Institute of Earth Sciences of the Academia Sinica of Taipei.

References

Christensen, U.R., 1984. Heat transport by variable viscosity convection and implications for the earth's thermal evolution. Phys. Earth Planet. Inter. 35, 264–282.
Christensen, U.R., Harder, H., 1990. 3-D convection with variable viscosity. Geophys. J. Int. 104, 213–226.
Davaille, A., Jaupart, C., 1993. Transient high-Rayleigh-number thermal convection with large viscosity variations. J. Fluid Mech. 253, 141–166.
Deschamps, F., Sotin, C., 2000. Inversion of two-dimensional numerical convection experiments for a fluid with a strongly temperature-dependent viscosity. Geophys. J. Int. 143, 204–218.
Deschamps, F., Sotin, C., 2001. Thermal convection in the outer shell of large icy satellites. J. Geophys. Res. 106, 5107–5121.
Deschamps, F., Mousis, O., Sanchez-Valle, C., Lunine, J.I., 2010a. The role of methanol on the crystallization of Titan's primordial ocean. Astrophys. J. 724, 887–894.
Deschamps, F., Tackley, P.J., Nakagawa, T., 2010b. Temperature and heat flux scalings for isoviscous thermal convection in spherical geometry. Geophys. J. Int. 182, 137–154.
Deschamps, F., Yao, C., Tackley, P.J., Sanchez-Valle, C., 2012. High Rayleigh number thermal convection in volumetrically heated spherical shells. J. Geophys. Res. 117, E09006. http://dx.doi.org/10.1029/2012JE004090.
Dumoulin, C., Doin, M.-P., Fleitout, L., 1999. Heat transport in stagnant lid convection with temperature- and pressure-dependent newtonian or non-newtonian rheology. J. Geophys. Res. 104, 12,759–12,777.
Durham, W.B., Stern, L.A., 2001. Rheological properties of water ice – application to satellites of outer planets. Annu. Rev. Earth Planet. Sci. 29, 295–330.
Durham, W.B., Kirby, S.H., Stern, L.A., 1997. Creep of water ices at planetary conditions: a compilation. J. Geophys. Res. 102, 16,293–16,302.
Fowler, A.C., 1985. Fast thermoviscous convection. Stud. Appl. Math. 72, 189–219.
Gerrard, J.A.F., Perutz, M.F., Roch, A., 1952. Measurement of the velocity distribution along a vertical line through a glacier. Proc. R. Soc. London (Ser. A) 207, 554–572.
Goldsby, D.L., Kohlstedt, D.L., 2001. Superplastic deformation of ice. J. Geophys. Res. 106, 11017–11030.
Goodman, D.J., Frost, H.J., Ashby, M.F., 1981. The plasticity of polycrystalline ice. Philos. Mag. A 43, 665–695.
Grasset, O., Parmentier, E.M., 1998. Thermal convection in a volumetrically heated, infinite Prandtl number fluid with strongly temperature dependent viscosity: implication for planetary thermal evolution. J. Geophys. Res. 103, 18171–18181.
Grasset, O., Sotin, C., 1996. The cooling rate of a liquid shell in Titan's interior. Icarus 123, 101–112.
Grasset, O., Sotin, C., Deschamps, F., 2000. On the internal structure and dynamics of Titan. Planet. Space Sci. 48, 617–636.
Hobbs, P.V., 1974. Ice Physics. Oxford University Press, p. 837.
Hussmann, H., Sohl, F., Spohn, T., 2006. Subsurface oceans and deep interiors of medium-sized outer planet and satellites and large trans-neptunian objects. Icarus 185, 258–273.
Labrosse, S., 2002. Hotspots, mantle plumes, and core heat loss. Earth Planet. Sci. Lett. 199, 147–156.
Lewis, J.S., 1971. Satellites of the outer planets: their physical and chemical nature. Icarus 15, 174–185.
McCord, T.B., Sotin, C., 2005. Ceres: evolution and current state. J. Geophys. Res. 110, E05009. http://dx.doi.org/10.1029/2004JE002244.
McKinnon, W.B., 2006. On convection in ice I shells of outer solar system bodies, with detailed application to Callisto. Icarus 183, 435–450.
Mitri, G., Showman, A.P., 2008. Thermal convection in ice-I shells of Titan and Enceladus. Icarus 193, 387–396.
Moore, B.W., 2008. Heat transport in a convecting layer heated from within and below. J. Geophys. Res. 113, B11407. http://dx.doi.org/10.1029/2006JB004778.
Moore, J.M., Pappalardo, R.T., 2001. Titan: an exogenic world? Icarus 212, 790–806.
Moore, D.R., Weiss, N.O., 1973. Two-dimensional Rayleigh–Bénard convection. J. Fluid Mech. 58, 289–312.
Moresi, L.-N., Solomatov, V.S., 1995. Numerical investigation of 2D convection with extremely large viscosity variations. Phys. Fluids 7, 2154–2162.
Morris, S., Canright, D., 1984. A boundary-layer analysis of Bénard convection in a fluid of strongly temperature-dependent viscosity. Phys. Earth Planet. Inter. 36, 355–373.
Mumma, M.J., Charnley, S.B., 2011. The chemical composition of comets-emerging taxonomies and natal heritage. Annu. Rev. Astron. Astrophys. 49, 471–524.
Ogawa, M., Schubert, G., Zebib, A., 1991. Numerical simulations of three-dimensional thermal convection in a fluid with strongly temperature-dependent viscosity. J. Fluid Mech. 233, 299–328.
Parmentier, E.M., Sotin, C., 2000. Three-dimensional numerical experiments on thermal convection in a very viscous fluid: implications for the dynamics of a thermal boundary layer at high Rayleigh number. Phys. Fluids 12, 609–617.
Reese, C.C., Solomatov, V.S., Baumgardner, J.R., 2005. Scaling laws for time-dependent stagnant lid convection in a spherical shell. Phys. Earth Planet. Inter. 149, 361–370.
Shahnas, M.H., Lowman, J.P., Jarvis, G.T., Bunge, H.-P., 2008. Convection in a spherical shell heated by an isothermal core and internal sources: implication for the thermal state of planetary mantles. Phys. Earth Planet. Inter. 168, 6–15.
Smolarkiewicz, P.K., 1984. A fully multidimensional positive definite advection transport algorithm with small implicit diffusion. J. Comput. Phys. 54, 325–362.
Solomatov, V.S., 1995. Scaling of temperature- and stress-dependent viscosity convection. Phys. Fluids 7, 266–274.
Solomatov, V.S., Moresi, L.-N., 2000. Scaling of time-dependent stagnant lid convection: application to small-scale convection on earth and other terrestrial planets. J. Geophys. Res. 105, 21795–21817.
Sotin, C., Labrosse, S., 1999. Three-dimensional thermal convection in an isoviscous, infinite Prandtl number fluid heated from within and from below: application to the transfer of heat through planetary mantles. Phys. Earth Planet. Inter. 112, 171–190.
Sotin, C., Grasset, O., Beauchesne, S., 1997. Thermodynamic properties of high pressure ices: Implications for the dynamics and internal structure of large icy satellites. In: Schmitt, B., et al. (Eds.), Solar System Ices, Springer, New-York, pp. 79–96.
Spohn, T., Schubert, G., 2003. Oceans in the icy Galilean satellites of Jupiter ? Icarus 161, 456–467.
Stengel, K.C., Oliver, D.S., Booker, J.R., 1982. Onset of convection in a variable-viscosity fluid. J. Fluid Mech. 120, 411–431.
Tackley, P.J., 2008. Modelling compressible mantle convection with large viscosity contrasts in a three-dimensional spherical shell using the yin-yang grid. Phys. Earth Planet. Inter. 171, 7–18.
Tarantola, A., Valette, B., 1982. Generalized nonlinear inverse problems solved using the least square criterion. Rev. Geophys. Space Phys. 20, 219–232.
Tobie, G., Mocquet, A., Sotin, C., 2005. Tidal dissipation within large icy satellites: applications to Europa and Titan. Icarus 177, 534–549.
Tobie, G., Choblet, G., Sotin, C., 2006. Tidally heated convection: constraints on Europa's ice shell thickness. J. Geophys. Res. 108. http://dx.doi.org/10.1029/2003JE002099.
Travis, B., Olson, P., 1994. Convection with internal sources and turbulence in the earth's mantle. Geophys. J. Int. 118, 1–19.
Travis, B., Olson, P., Schubert, G., 1990. The transition from two-dimensional to three-dimensional planforms in infinite Prandtl number thermal convection. J. Fluid Mech. 216, 71–91.
Weertman, J., 1983. Creep deformation of ice. Annu. Rev. Earth Planet. Sci. 11, 215–240.
Wesseling, P., 1992. An Introduction to Multigrid Methods. John Wiley and Sons, p. 284.
White, D.B., 1988. The planforms and onset of convection with a temperature-dependent viscosity. J. Fluid Mech. 191, 247–286.